

A Latent Implicit 3D Shape Model for Multiple Levels of Detail

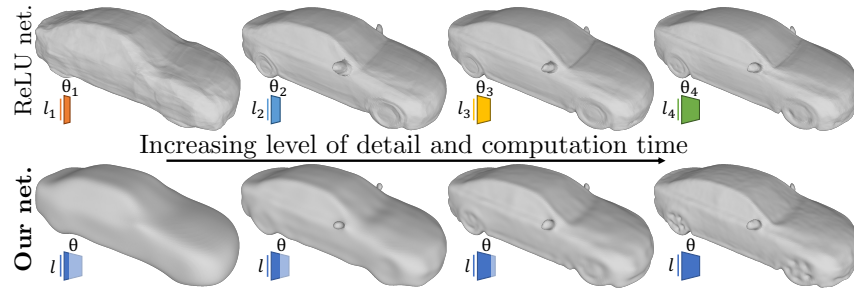
Benoit Guillard¹, Marc Habermann², Christian Theobalt², and Pascal Fua¹

¹ CVLab, EPFL, Switzerland {benoit.guillard, pascal.fua}@epfl.ch

² Max Planck Institute for Informatics, Saarland Informatics Campus, Germany
{mhaberma, theobalt}@mpi-inf.mpg.de

Abstract. Implicit neural representations map a shape-specific latent code and a 3D coordinate to its corresponding signed distance (SDF) value. However, this approach only offers a single level of detail. Emulating low levels of detail can be achieved with shallow networks, but the generated shapes are typically not smooth. Alternatively, some network designs offer multiple levels of detail, but are limited to overfitting a single object.

To address this, we propose a new shape modeling approach, which enables multiple levels of detail and guarantees a smooth surface at each level. At the core, we introduce a novel latent conditioning for a multiscale and bandwidth-limited neural architecture. This results in a deep parameterization of multiple shapes, where early layers quickly output approximated SDF values. This allows to balance speed and accuracy within a single network and enhance the efficiency of implicit scene rendering. We demonstrate that by limiting the bandwidth of the network, we can maintain smooth surfaces across all levels of detail. At finer levels, reconstruction quality is on par with the state of the art models, which are limited to a single level of detail.



Implicit neural shape representations map latent codes to 3D surfaces using a neural network. **Top:** traditional networks can only reconstruct shapes at one level of detail (LoD). To model increasing LoDs, networks must be made deeper (θ_1 to θ_4). These networks do not share their latent codes l_i , and yield rough surfaces when shallow ($i = 1$). **Bottom:** we propose to use a single network θ to map the same latent code l to multiple LoDs. Lower LoDs are quickly provided by the early layers of the network. We restrict their bandwidths with a new network design to reconstruct smoother shape approximations at low LoD.

1 Introduction

Latent implicit shape representations [24,22,16,2,19] have become increasingly important for 3D shape modeling. They learn a parametric representation of 3D shapes in the form of latent vectors. They streamline the modeling process, by reducing it to finding a single latent vector. However, they only provide a single level of detail (LoD) and sometimes produce unnecessarily bumpy surfaces when using shallow network architectures. This is regrettable because LoD control allows to balance computational speed and surface precision. For instance, in 3D scene rendering, objects that are far away from the virtual camera do not require high geometric details. Similarly, smooth surfaces benefit many downstream applications as they allow for more natural shading and better rendering.

The most trivial way to represent implicit shapes at multiple LoD is to simply use shallower networks. This requires one network per level of detail, each of them with different latent spaces. Instead, our goal is that multiple LoD share the same latent space. Therefore, we start from an existing multiscale and band-limited architecture [20] that ensures that geometric details at certain layers do not exceed a given frequency, but is designed to model a single signal. We show how it can be extended to provide a latent representation for 3D surfaces while preserving its band-limited properties, which ensures smooth surfaces at all LoD. With our design, early layers quickly provide reasonable shape estimates and later layers simply add more details, which makes it easy to select the desired level of detail for any potential application. We explain how this can be exploited to quickly explore the shape space in an interactive manner.

In summary, our contributions are as follows:

- We propose the first latent and implicit method, which supports multiple level of details and guarantees surface smoothness.
- To this end, we introduce latent conditioning to a multiscale and band-limited neural network architecture, while preserving its band-limiting property.
- We also introduce a joint optimization of the frequency and phase parameters of each positional encoding layer, resulting in higher quality shape models.
- We demonstrate efficient latent space exploration for interactive shape editing and design.

Our experiments demonstrate that the proposed method significantly improves the smoothness across all LoD of the surface while demonstrating a geometric quality that is on par with the current state of the art implicit shape modeling methods, which do not support multiple levels of detail. We will release code upon acceptance.

2 Related Work

Implicit neural shape representations were first introduced in DeepSDF [24] and Occupancy networks [22]. These representations use a fully connected network to map a latent code to a 3D scalar field, which is converted to a watertight

shape by extracting its isosurface with Marching Cubes [18]. They were originally only suitable for watertight surfaces, but later extended to unsigned distance fields [5,44,11]. These representations have been applied in various tasks, such as single view reconstruction of objects [38] and humans [29,30] from images or point clouds [25]. They were also improved with regards to various aspects, such as the smoothness of the latent space [21] or the physical plausibility of the output shapes [23]

Furthermore, part-wise representations have been obtained by splitting the latent code in 3D space [16,2,19], and transformer layers have been applied to refine these part-wise 3D latent codes [13,42]. Despite providing very accurate reconstructions, they only provide one level of detail, and no longer provide shape parameterizations from a single vector. In comparison, our network relies on a compact latent code, which enables shape recovery and manipulation in the presence of an incomplete signal [28].

Multiple levels of detail for 3D shapes are traditionally obtained by post-processing meshes [14,15,37,43]. By contrast, to save computations, we aim at achieving variable LoD from the implicit network itself, before meshing the implicit signal. Variable LoD have already been incorporated into implicit networks, but none of them learn a latent shape model. One approach is to store latent codes at multiple levels of an octree, which are then decoded with a shared network to provide multiple levels of detail, as in NGLOD [34]. Another approach is BACON [20], which stores implicit signals at multiple levels of detail within the weights of a single network. It is using a specific band-limited architecture [8] to progressively improve coarse approximations [20] with each layer. The residual formulation of [31] improves its performance on hierarchical optimizations problems, and it has been extended in [39] to impose lower bounds on bandwidth and specific phases for the signal. SAPE [12] also learns variable frequency encodings, and [33] demonstrates high compression rates of neural radiance fields using vector quantization. However, as BACON, they remain limited to overfitting a single signal. Some studies have attempted to guide the training of implicit networks by gradually increasing the level of detail during training [6], but they remain limited to one level at inference. Closer to our work is MDIF [4], which learns a multiscale representation on a grid of codes and uses a drop-out strategy for enabling shape completion. This requires writing per-task regularization losses when full volumetric supervision is not available for unseen shapes. By contrast, our representation is more versatile since it relies on a single latent code.

New architectures departing from standard fully connected networks have been proposed for implicit networks, to tailor them to the task at hand. For instance, activation functions can be replaced by Gaussian in implicit networks [26], and SIREN [32] uses periodic activations in conjunction with a hypernetwork to learn a shape prior. Dupont et al. [7] take a different approach by using a SIREN network modulated by latent codes to learn shape priors, which enables a single network to represent multiple shapes. SIREN is also used in [41], which combines two networks to learn an SDF from a point cloud input, representing a coarse shape and higher frequency displacements. Our work also departs from

standard fully connected networks, with the aim of jointly achieving conditioning on a latent code and imposing band-limiting at multiple scales.

3 Method

Our goal is to learn an implicit shape model from a collection of 3D shapes of a specific category, e.g. cars or chairs, which supports *multiple levels of detail* and at each level *smoothness* is also guaranteed. We learn a function

$$f_{\Omega}(\mathbf{x}, \mathbf{l}, i) = s \quad (1)$$

predicting the signed distance value $s \in \mathbb{R}$, where $\mathbf{x} \in \mathbb{R}^3$ is a query point in 3D space, $\mathbf{l} \in \mathbb{R}^{d_l}$ is a latent code for modeling the shape, $i \in \{1, \dots, N-1\}$ is the desired level of detail, and Ω are the learnable parameters of the network. Inspired by BACON [20], we first recap how a band-limited network architecture can implement a simplified version of the above function, i.e. $f_{\Omega}(\mathbf{x}, i)$, where latent conditioning and therefore modeling different shapes is not possible (Sec. 3.1). Next, we discuss multiple possible solutions for introducing a latent conditioning to this type of architecture and provide an analysis why only one of the proposed designs can accomplish this goal while preserving the original properties of band-limited networks (Sec. 3.2). To achieve a higher shape accuracy, we further introduce a joint learning of per-layer frequencies and phases (Sec. 3.3). By exploiting the multiple levels of detail, we then introduce an interactive latent space exploration enabling efficient shape manipulation (Sec. 3.4). Last, we provide details for the training and inference procedures (Sec. 3.5).

3.1 Band-limited Coordinate Network

A BACON network [20] with N layers maps an input coordinate $\mathbf{x} \in \mathbb{R}^3$ to $N-1$ estimates of the SDF at this position, $f_{\Omega}(\mathbf{x}, i)$ with $1 \leq i < N$. The input coordinate $\mathbf{x} \in \mathbb{R}^3$ is first encoded using sine layers

$$\mathbf{g}_i(\mathbf{x}) = \sin(\boldsymbol{\omega}_i \mathbf{x} + \boldsymbol{\phi}_i) \in \mathbb{R}^{d_h} \quad (2)$$

for $i = 0, \dots, N-1$, with *frequencies* $\boldsymbol{\omega}_i \in \mathbb{R}^{d_h \times 3}$, *phase shifts* $\boldsymbol{\phi}_i \in \mathbb{R}^{d_h}$, and d_h the hidden dimension. Intermediate activations $\mathbf{z}_i \in \mathbb{R}^{d_h}$ and SDF outputs $f_{\Omega}(\mathbf{x}, i) \in \mathbb{R}$ are

$$\begin{aligned} \mathbf{z}_0 &= \mathbf{g}_0(\mathbf{x}) \text{ and } \mathbf{z}_i = \mathbf{g}_i(\mathbf{x}) \circ (\mathbf{W}_i \mathbf{z}_{i-1} + \mathbf{b}_i), \quad 1 \leq i < N \\ f_{\Omega}(\mathbf{x}, i) &= \mathbf{W}_i^{\text{out}} \mathbf{z}_i + \mathbf{b}_i^{\text{out}} \end{aligned} \quad (3)$$

where \circ is the Hadamard product, $(\mathbf{W}_i, \mathbf{b}_i) \in (\mathbb{R}^{d_h \times d_h} \times \mathbb{R}^{d_h})$ are the *linear layers* and $(\mathbf{W}_i^{\text{out}}, \mathbf{b}_i^{\text{out}}) \in (\mathbb{R}^{1 \times d_h} \times \mathbb{R})$ are the *output layers*. The learnable parameters of the network $\Omega = \{\mathbf{W}_i, \mathbf{b}_i, \mathbf{W}_i^{\text{out}}, \mathbf{b}_i^{\text{out}}\}$ are overfit to a single SDF signal.

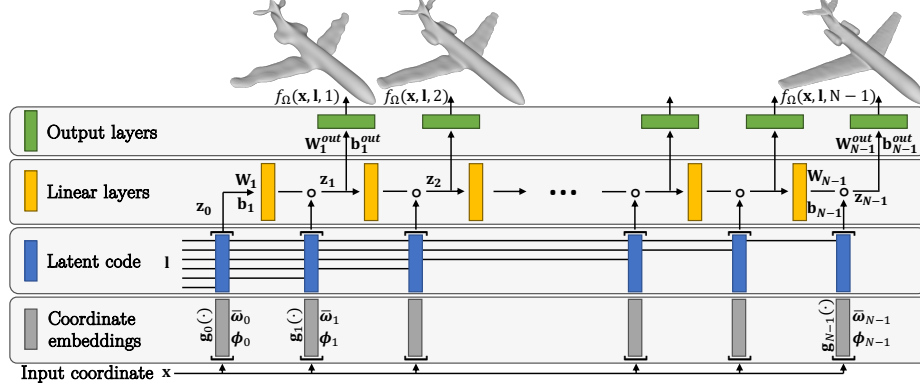


Fig. 1: **Network Architecture.** coordinate \mathbf{x} is encoded with parametric functions $\mathbf{g}_i(\cdot)$, and concatenated with the latent code \mathbf{l} . Linear layers ($\mathbf{W}_i, \mathbf{b}_i$) and hadamard products yield the intermediate activations \mathbf{z}_i . At level i , the SDF output is predicted with the output layer ($\mathbf{W}_i^{\text{out}}, \mathbf{b}_i^{\text{out}}$). All network parameters $\Omega = \{\mathbf{W}_i, \mathbf{b}_i, \mathbf{W}_i^{\text{out}}, \mathbf{b}_i^{\text{out}}, \overline{\omega}_i, \phi_i\}$ are optimized jointly with the latent codebook.

Frequency coefficients ω_i are sampled uniformly in $[-B_i, B_i]$, with $B_i > 0$, and in $[-\pi, \pi]$ for phases ϕ_i ,

$$\omega_i \sim \mathcal{U}([-B_i, B_i]^{d_h \times 3}), \quad \phi_i \sim \mathcal{U}([-\pi, \pi]^{d_h}). \quad (4)$$

Applying the trigonometric property $2 \sin(a) \sin(b) = \sin(a+b-\frac{\pi}{2}) + \sin(a-b+\frac{\pi}{2})$ repeatedly to the Hadamard products of Eq. (3), [8,20] demonstrate that the output signal $f_\Omega(\cdot, i)$ of layer i has its bandwidth upper-bounded by $\sum_{j=0}^i B_j$. In other words, since multiplying sines sums their frequencies, this network design ensures that the maximum spatial frequency of the output SDFs is increasing with depth. As a result, (i) the first SDF outputs are smooth by construction, and (ii) the SDF fields $f_\Omega(\cdot, i)$ can represent more details as i increases. This increase is controlled by the bounds B_i of Eq. (4) and can be manually tuned.

3.2 Conditional Band-limited Network

The network described above can only overfit a single SDF field, and, thus, represents a single shape as its 0-level set. Our aim is to extend it to represent multiple geometries with a single network, by conditioning it on a shape specific latent code $\mathbf{l} \in \mathbb{R}^{d_l}$. Although the BACON architecture effectively guarantees band-limited SDF outputs with respect to spatial coordinates, it is also a very constraining architecture that makes it challenging to incorporate a latent code. Consequently, in the remainder of this chapter, we explore and discuss three different alternatives for latent conditioning (see also Fig. 2).

Design 1. The most trivial suggestion is to simply concatenate \mathbf{l} with the input coordinates \mathbf{x} , i.e. Eq. (2), becomes

$$\mathbf{g}_i(\mathbf{x}) = \sin(\omega_i[\mathbf{x} \parallel \mathbf{l}] + \phi_i) \in \mathbb{R}^{d_h},$$

where $[\cdot|\cdot]$ is the concatenation of 2 vectors. As shown in Fig. 2, it fails to learn discernible shapes as it results in band-limiting the SDF with respect to the latent space, which is neither desired nor relevant to our objectives.

Design 2. Another approach is to append \mathbf{l} at every output layer, i.e. by updating Eq. (3) as $f_{\Omega}(\mathbf{x}, \mathbf{l}, i) = \mathbf{W}_i^{out}[\mathbf{z}_i|\mathbf{l}] + \mathbf{b}_i^{out}$. As shown in Fig. 2, cars are identifiable, but far from their ground truth and almost identical to one another. We explain it by noticing that most of the network’s computations are shared by all the different geometries, which have the same hidden layers \mathbf{z}_i values. As a result, this only adds a fixed SDF offset for each latent code \mathbf{l} . Equivalently, \mathbf{l} only varies the reconstructed level set of a scalar field that is fixed for all shapes.

Design 3. The third approach is to append \mathbf{l} to all the hidden layers \mathbf{z}_i . As shown in Fig. 2, this is the most effective solution, which we adopt. More specifically, we concatenate \mathbf{l} to the sinus embeddings of spatial coordinates, and the network formulation in Eq. (3) becomes

$$\begin{aligned} \mathbf{z}_0 &= [\mathbf{g}_0(\mathbf{x}) \mid \mathbf{l}] \text{ and } \mathbf{z}_i = [\mathbf{g}_i(\mathbf{x}) \mid \mathbf{l}] \circ (\mathbf{W}_i \mathbf{z}_{i-1} + \mathbf{b}_i) \\ f_{\Omega}(\mathbf{x}, \mathbf{l}, i) &= \mathbf{W}_i^{out} \mathbf{z}_i + \mathbf{b}_i^{out}, \quad 1 \leq i < N. \end{aligned} \quad (5)$$

This architecture is graphically laid out in Fig. 1. To accommodate for the addition of a latent vector, the dimension of the linear and output layers is increased from d_h to $d_h + d_l$. For a fixed latent \mathbf{l} , Eq. (5) can be rewritten into Eq. (3) with simple matrix manipulations. As a result, each SDF $f_{\Omega}(\cdot, \mathbf{l}, i)$ is bounded by $\sum_{j=0}^i B_j$ in the frequency domain, and this new latent architecture preserves the band-limiting property of Eq. (3).

3.3 Adjusting Bounded Frequencies

Throughout our experiments (see Sec. 4.5), we found that the parameters of the coordinate embedding layers of Eq. (2) play a crucial role for the overall surface detail, and even more importantly optimal parameters highly vary for different shape categories. Thus, we optimize the frequencies ω_i and phase shifts ϕ_i instead of fixing them to their initial random uniform values of Eq. (4). In order to maintain the band limiting properties of the network, coefficients of ω_i must be restricted to the fixed range $[-B_i, B_i]$. We thus, re-parametrize it as $\omega_i = \tanh(\overline{\omega}_i) * B_i$ and optimize $\overline{\omega}_i \in \mathbb{R}^{d_h \times 3}$ instead. Coefficients ϕ_i do not require such a re-parameterization and can be freely optimized, due to the periodicity of the $\sin(\cdot)$ function. We add $\overline{\omega}_i$ and ϕ_i to the network’s learnable parameters, which become $\Omega = \{\mathbf{W}_i, \mathbf{b}_i, \mathbf{W}_i^{out}, \mathbf{b}_i^{out}, \overline{\omega}_i, \phi_i\}$.

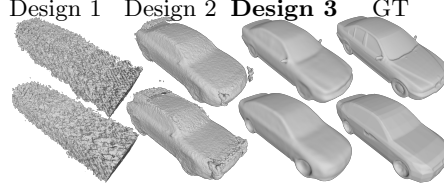


Fig. 2: **Architecture Design.** When concatenating a latent code to the input coordinates (**Design 1**) or the output layers (**Design 2**), the resulting shapes are unsatisfactory. When the latent code is concatenated to the hidden layers (**Design 3 (Ours)**), the generated shapes are significantly closer to the ground truth.

3.4 Efficient Latent Space Exploration

This network architecture provides important benefits for interactive latent space exploration. Running the early layers of the network can provide a coarse, but smooth shape approximation. To obtain the mesh $M_i(\mathbf{l})$ at level i for a given latent code \mathbf{l} , we apply Marching Cubes [18] to $f(\cdot, \mathbf{l}, i)$. To accelerate iso-surface extraction, we use an octree structure, similar to [22,36,10]. Initially, the SDF field $f(\cdot, \mathbf{l}, i)$ is evaluated on a low-resolution regular grid (of shape 32^3), which is then subdivided only for cells where the predicted value is smaller than the grid size. The SDF is subsequently queried at higher grid resolutions iteratively until we reach the desired resolution (typically 256^3). This approach, combined with a low number of network layers, allows for rapidly obtaining a mesh, and real time exploration of the latent space.

To increase the level of detail and manipulate the mesh $M_{i'}$ with $i' > i$, we use the same latent code \mathbf{l} . This differs from a naive solution employing multiple networks with various depths, which would not share their latent spaces. To accelerate iso-surface extraction for level i' , we re-employ SDF estimates from level i , following [20]. We only query $f(\cdot, \mathbf{l}, i')$ at grid voxels where $|f(\cdot, \mathbf{l}, i)|$ is smaller than a threshold τ . This results in fewer operations than filling the octree from scratch with $f(\cdot, \mathbf{l}, i')$, and, thus, a faster mesh recovery.

3.5 Network Training and Inference

We train our network in the auto-decoder fashion [24]. Given a dataset \mathcal{D} of watertight training shapes, we jointly optimize the network parameters Ω and a latent codebook $\mathbf{L} \in \mathbb{R}^{|\mathcal{D}| \times d_l}$ containing one code per shape. Training is performed by minimizing the sum of a loss on predicted SDF values \mathcal{L}_{sdf} and a regularization term \mathcal{L}_{reg} as $\min_{\Omega, \mathbf{L}} \mathcal{L}_{\text{sdf}} + \mathcal{L}_{\text{reg}}$.

SDF Loss. The SDF of the j -th training shape is sampled S_f times close to the surface to provide *fine* ground truth samples $(\dot{s}_k^j, \dot{\mathbf{x}}_k^j) \in (\mathbb{R} \times \mathbb{R}^3)$ with $k = 1, \dots, S_f$, and S_c times further away from the surface for *coarse* ground truth samples $(\ddot{s}_k^j, \ddot{\mathbf{x}}_k^j) \in (\mathbb{R} \times \mathbb{R}^3)$. We sum the squared distances between ground truth and predicted SDFs

$$\mathcal{L}_{\text{sdf}} = \left\| \dot{s}_k^j - f_{\Omega}(\dot{\mathbf{x}}_k^j, \mathbf{L}_j, i) \right\|_2^2 + \lambda_c \left\| \ddot{s}_k^j - f_{\Omega}(\ddot{\mathbf{x}}_k^j, \mathbf{L}_j, i) \right\|_2^2 \quad (6)$$

at each network depth i , for each training shape j , and each SDF sample k . We follow [20,6] and apply a lower weight $\lambda_c < 1$ to samples that are far from the surface. Notice that all LoDs i are supervised with the same ground truth SDF. No pre-processing (such as smoothing) is required for low LoDs, which are band-limited by the network architecture.

Regularization Loss. As in [24], we add an L_2 regularizer \mathcal{L}_{reg} on latent codes, with weight λ_{reg} .

Inference. To test a network after training, we solve for the latent codes of unseen objects that best fit their SDFs. The trained network parameters are frozen and act as a learned geometric prior [24]. We optimize with gradient descent one latent code per unseen shape by minimizing $\mathcal{L}_{\text{sdf}} + \mathcal{L}_{\text{reg}}$.

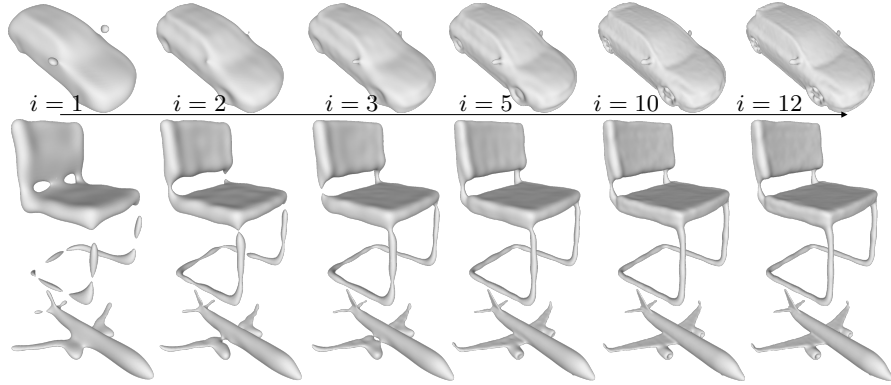


Fig. 3: **Test Shape Reconstructions** with varying levels of detail. The lowest possible level of detail ($i = 1$) is smooth and already captures a very coarse structure of the shape. As i increases, more details appear (up to saturation).

4 Experiments

We first demonstrate that our model is able to learn a parameterization of shapes that share geometric attributes and construct a coarse-to-fine hierarchy of details. Secondly, we provide a quantitative comparison of our model to the most performant baselines, which demonstrates that our model is as accurate while exhibiting better behavior, and allowing to balance precision and computation time with a single network. Lastly, we perform an ablation study to understand the significance of optimizing the coordinate embedding parameters ω_i and ϕ_i .

4.1 Setting

Datasets. We use 3 object categories from ShapeNet [3]: cars, chairs and airplanes, all normalized to fill 90% of a $[-0.5, 0.5]^3$ bounding box. For each of them, we train separate networks using 1200 shapes, and test them on 110 unseen shapes.

Hyperparameters. We train networks with $N = 13$ layers, resulting in 12 SDF outputs of increasing frequencies. We set the maximum spatial frequency to $B = \sum_i B_i = 256$, latent codes to a size of $d_l = 256$ and coordinate embeddings to $d_h = 256$. For testing the network, we optimize an initial latent code $\mathbf{l} = 0 \in \mathbb{R}^{d_l}$ for 1000 steps with Adam [17], decreasing the learning rate linearly from 10^{-3} to 10^{-5} between steps 900 and 1000.

4.2 Learning a Multiscale Shape Parameterization

In Fig. 3, we qualitatively demonstrate our model’s ability to memorize training shapes and acquire a valuable prior to fit novel shapes. The band-limited outputs progressively capture finer details throughout the network, leading to a learned hierarchy of details. We observe that details seem to reach saturation for the last

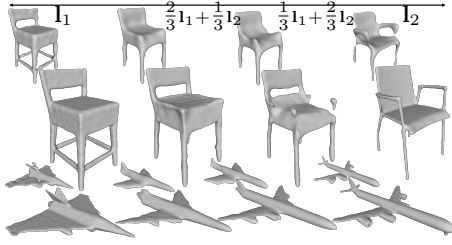


Fig. 4: **Linear Interpolation** in the latent space translates into smooth shape deformations. Smaller objects correspond to a lower level of detail ($i = 1$), shown in the insets, this captures surface and follow a similar transformation to the more detailed ones ($i = 12$).

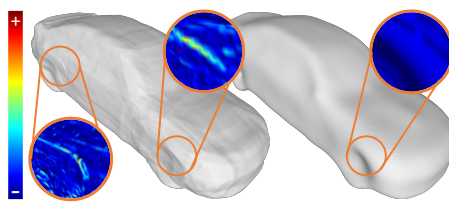


Fig. 5: **Surface Regularity (SR)**: to measure regularity we average the vertex displacements that one step of Laplacian smoothing would cause. As shown in the insets, this captures surface cracks and bumps (left: 1 layer *ReLU-net*, right: ours at $i = 1$).

layers, which is further confirmed through quantitative assessment. Despite not always preserving topology, low levels of detail capture the shape outlines.

Interpolation in the Latent Space. Fig. 4 illustrates the outcome of linear interpolation between two known latent codes and shows that the learned shape embedding is both continuous and complete. Despite using unconventional activation functions on the latent codes, our novel architecture effectively represents meaningful shape abstractions, and also allows for seamless topology changes.

4.3 Shape Accuracy and Smoothness

Metrics. For measuring the faithfulness of the reconstructed surfaces, we use:

- The Chamfer Distance (CD) on 10k points on the reconstructed and ground truth surfaces, multiplied by 10^5 . Lower values mean higher accuracy.
- The Earth mover’s Distance (ED) for 5k surface points, using GeomLoss [9] and multiplied by 10^4 . Again, lower distances imply better reconstruction.

For quantifying Surface Regularity (SR), we compute the average norm of each vertex displacement induced by one step of Laplacian smoothing, as shown in Fig. 5. The lower, the smoother the surface. This metric is not computed with regards to a ground truth mesh, but is a per-shape score.

Baselines. We compare our pipeline to other network architectures that rely on a compact latent code to represent shapes. For them, we use another natural way of limiting the level of details, which consists in reducing the depth of a standard network, and, thus, its capacity. We implement a ReLU network, with DeepSDF’s architecture [24] and positional encoding [35] of degree 8, and refer to it as *ReLU-net*. We also implement a version of SIREN [32]. To learn geometric priors instead of overfitting a single shape, we condition it on latent codes via modulating layers, as in [7]. It uses sinus activations, and we refer to it as *Sin-net*. For each baseline, we train 12 networks, with depths ranging from 1 to 12. We use the same hidden and latent sizes (512, 256) as for our network.

Accuracy. Tab. 1 compares our network with two baseline models, *ReLU-net* and *Sin-net*, for depths $i = 2, 4, 8, 12$ on the test splits for all three shape

	Layer #:	2			4			8			12		
	Metric	CD	ED	SR	CD	ED	SR	CD	ED	SR	CD	ED	SR
Cars	<i>Sin-net</i>	7.9	3.9	9.5	6.8	3.5	9.9	10.5	3.5	9.7	10.8	3.5	9.6
	<i>ReLU-net</i>	7.7	2.9	11.2	6.0	2.8	10.9	6.3	2.7	10.9	6.1	2.7	11.4
	Ours	8.1	3.2	5.5	7.0	2.9	6.1	6.3	2.8	7.1	6.3	2.8	7.3
Chairs	<i>Sin-net</i>	14.9	5.0	13.0	13.4	4.6	12.0	10.7	4.9	16.0	12.7	6.4	19.0
	<i>ReLU-net</i>	10.0	3.9	13.0	9.1	3.7	12.4	8.8	3.6	12.5	9.3	3.6	13.2
	Ours	14.3	5.4	7.8	10.1	4.0	7.8	8.3	3.4	8.3	8.3	3.4	8.4
Planes	<i>Sin-net</i>	4.5	3.3	14.0	3.6	2.5	13.7	2.9	2.1	14.7	5.2	3.4	16.1
	<i>ReLU-net</i>	3.0	2.0	15.0	2.7	2.0	14.5	2.6	1.8	15.5	2.4	1.6	14.8
	Ours	5.8	3.0	12.2	3.8	2.3	13.0	2.7	1.5	14.1	2.7	1.5	14.5

Table 1: **Unseen Test Shapes:** Chamfer Distances (CD), Earth mover’s Distances (ED) and Surface Regularity (SR) – lower values indicate better results. We achieve comparable best (CD, ED) while being smoother (SR) than the best baseline (*ReLU-net*). *Sin-net* and *ReLU-net* require training one network per category and LoD ours simply needs per-category training.

categories. Our method achieves minimal ED and CD scores that are very similar to *ReLU-net* and consistently better than *Sin-net*. This validates that our network representation of 3D surfaces is comparable to the best baselines in terms of accuracy. Fig. 6 shows a qualitative comparison.

In Fig. 7 (top), we plot reconstruction accuracy (ED) as a function of network depth for our single network and 12 *ReLU-net* networks of varying depths for the cars and chairs datasets. The error monotonously decreases with depth for our solution, which is not the case for *ReLU-net*. Therefore, band-limiting makes our solution more consistent and predictable. This also highlights another practical benefit of a single network approach: it can be pruned after training. By discarding layers $i > 8$, we avoid manual hyperparameter tuning and get the best performance with a single training.

It is worth noting that *ReLU-net* and *Sin-net* require one network for each depth, resulting in one latent code per depth for encoding each shape. It could imaginably be possible to train these models with a shared latent space, or with one SDF head per layer. They would however still exhibit a greater degree of surface irregularity, which we explain in more detail below.

Surface Regularity. Across all object categories and depths, our network consistently achieves lower SR values, as shown in Tab. 1. This indicates that the shapes generated by our network are always smoother than those generated by *ReLU-net* and *Sin-net*. This trend holds at higher levels of detail, with almost equal ED and CD values.

Moreover, our pipeline allows for an explicit and controllable trade-off between shape accuracy (ED) and surface regularity (SR). As demonstrated in Fig. 7 (bottom), there is a very consistent trend: as the output layer becomes deeper, accuracy improves while smoothness decreases. In contrast, *ReLU-net* does not exhibit such a correlation.

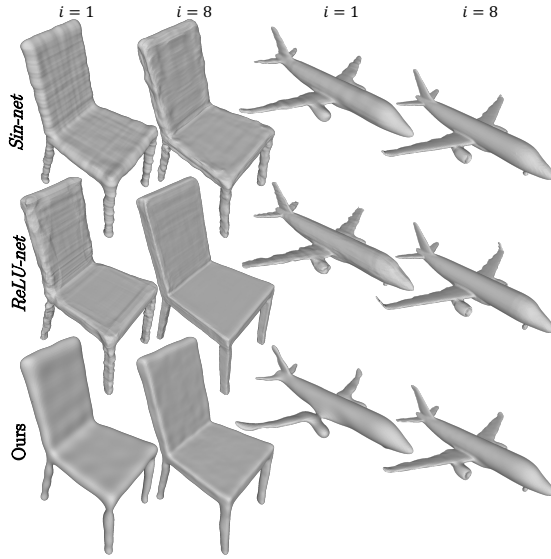


Fig. 6: **Unseen Test Shapes** as reconstructed by our model, *Sin-net* and *ReLU-net*. It is visible on flat regions of the chair that our model provides smoother surfaces at lower LoD ($i = 1$).

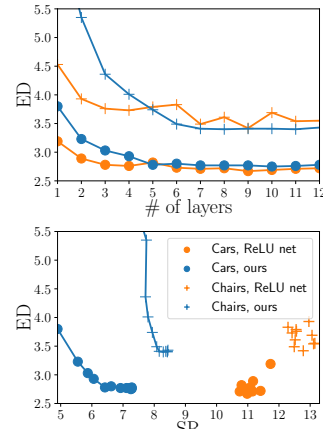


Fig. 7: **Earth mover's Distance (ED)**. **Top:** ED as a function of depth. *ReLU-nets* (1 per depth) are less monotonous than *ours* (single network). **Bottom:** *Ours* exhibits a clear tradeoff between ED/SR, but not *ReLU-nets*.

4.4 Shape Reconstruction Speed

At level $i = 8$, reconstructing a mesh at resolution 256 using the octree subdivision method described in [22,36,10] takes an average of **66.7ms** on an Nvidia A100 GPU, of which only 3.4ms is spent on Marching Cubes [40]. It is reduced to **58.9ms** by early stopping the network computations when $|f(\cdot, \cdot, i')| > \tau$ with $i' < 8$, as suggested in [20] and explained in Sec. 3.4. This reduction in computation time is a significant advantage of the multiscale network architecture, which provides coarse SDF estimates in just a few operations.

Furthermore, our network can adaptively balance computation time and precision. This proves useful for meshing and rasterizing a collection of implicit objects, and rendering an image of a 3D scene as depicted in Fig. 8. By using coarse LoD ($i < 4$) for distant objects while maintaining high quality for nearby ones, we can render the scene much faster than a *ReLU-net*.

4.5 Ablations

	CD	ED
Ours	8.3	3.4
Fixed ω	8.9	3.6
Fixed ϕ	8.7	3.5
Fixed ω and ϕ	9.0	3.5

We perform an ablation on the optimization of the coordinate embedding parameters ω and ϕ in our approach. We analyze the performance on test chairs at a depth of $i = 8$ when these parameters are left fixed to their initial values. As shown in the inset table, there is a moderate drop in performance when these parameters are not optimized.

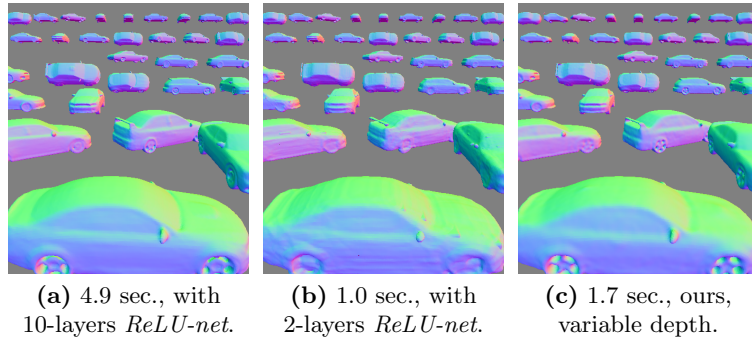


Fig. 8: **Meshing and rasterizing implicit shapes:** (a) A deep *ReLU-net* provides details but is slow. (b) A shallower *ReLU-net* is fast but coarse. (c) With ours, network depth and LoD can be adjusted based on camera distance, to render quickly and without artifacts.

In another experiment, we trained on chairs, but freezing ω and ϕ to the ones obtained by training on cars. This resulted in a 15% increase of ED, again demonstrating the importance of learning category specific frequencies and phases.

4.6 Shape Completion

In Fig. 9, we showcase our network’s capability to reconstruct shapes based on partial SDF signals. The gradient descent procedure we employ is similar to the one used for the previous section, but this time the SDF supervision is limited to only half of the 3D domain. Despite the reduced supervision, our pipeline successfully recovers valid shapes that adhere to the provided SDF signal, while also generating plausible completions in regions lacking supervision. By employing a single latent code to parameterize the entire 3D distance field, our network acts a strong shape prior.



Fig. 9: **Shape Completion** Our network can complete unseen 3D shapes even when the SDF signal is incomplete. In these examples, only the red half of the object received SDF supervision, yet the compact latent code parameterization yields entire shapes.

5 Conclusion

We propose a novel latent conditioned architecture for implicit 3D shape representation with multiple levels of details, and enable explicit control of the SDF maximum frequency for each level. This architecture is a learned shape parameterization from a single latent vector. Our experiments demonstrate that, at the highest level of detail, it is just as accurate as other existing methods, while consistently producing smoother results with fewer surface artifacts at lower

levels of detail. Additionally, it offers a controllable tradeoff between speed and accuracy.

We will investigate a disentangled latent representation for each LoD, which would enable mix-and-matching coarse outlines and local details. This would allow for greater flexibility and control over the generation of 3D shapes.

Acknowledgments

This work was supported in part by the Swiss National Science Foundation. Christian Theobalt was supported by ERC Consolidator Grant 4DReply (770784).

References

1. Atzmon, M., Lipman, Y.: SALD: Sign Agnostic Learning with Derivatives. In: International Conference on Learning Representations (2020)
2. Chabra, R., Lenssen, J., Ilg, E., Schmidt, T., Straub, J., Lovegrove, S., Newcombe, R.: Deep Local Shapes: Learning Local SDF Priors for Detailed 3D Reconstruction. In: European Conference on Computer Vision (2020)
3. Chang, A., Funkhouser, T., G., L., Hanrahan, P., Huang, Q., Li, Z., Savarese, S., Savva, M., Song, S., Su, H., Xiao, J., Yi, L., Yu, F.: Shapenet: An Information-Rich 3D Model Repository. In: arXiv Preprint (2015)
4. Chen, Z., Zhang, Y., Genova, K., Funkhouser, T., Fanello, S., Bouaziz, S., Haene, C., Du, R., Keskin, C., Tang, D.: Multiresolution Deep Implicit Functions for 3D Shape Representation. In: International Conference on Computer Vision (2021)
5. Chibane, J., Mir, A., Pons-Moll, G.: Neural Unsigned Distance Fields for Implicit Function Learning. In: Advances in Neural Information Processing Systems (2020)
6. Duan, Y., Zhu, H., Wang, H., Yi, L., Nevatia, R., Guibas, L.J.: Curriculum DeepSDF. In: European Conference on Computer Vision (2020)
7. Dupont, E., Kim, H., Eslami, S.A., Rezende, D.J., Rosenbaum, D.: From data to functa: Your data point is a function and you can treat it like one. In: International Conference on Machine Learning (2022)
8. Fathony, R., Sahu, A.K., Willmott, D., Kolter, J.Z.: Multiplicative filter networks. In: International Conference on Learning Representations (2021)
9. Feydy, J., Roussillon, P., Trouvé, A., Gori, P.: Fast and scalable optimal transport for brain tractograms. In: Conference on Medical Image Computing and Computer Assisted Intervention (2019)
10. Guillard, B., Remelli, E., Lukoianov, A., Richter, S., Bagautdinov, T., Baque, P., Fua, P.: Deepmesh: Differentiable Iso-Surface Extraction. In: arXiv Preprint (2022)
11. Guillard, B., Stella, F., Fua, P.: MeshUDF: Fast and Differentiable Meshing of Unsigned Distance Field Networks. In: European Conference on Computer Vision (2022)
12. Hertz, A., Perel, O., Giryes, R., Sorkine-Hornung, O., Cohen-Or, D.: Sape: Spatially-adaptive progressive encoding for neural optimization. Advances in Neural Information Processing Systems (2021)
13. Hertz, A., Perel, O., Giryes, R., Sorkine-Hornung, O., Cohen-Or, D.: Spaghetti: Editing implicit shapes through part aware generation. ACM Transactions on Graphics (2022)

14. Hoppe, H.: Progressive meshes. In: ACM SIGGRAPH (1996)
15. Hoppe, H.: View-dependent refinement of progressive meshes. In: Proceedings of the ACM on Computer Graphics and Interactive Techniques (1997)
16. Jiang, C., Sud, A., Makadia, A., Huang, J., Nießner, M., Funkhouser, T., et al.: Local implicit grid representations for 3d scenes. In: Conference on Computer Vision and Pattern Recognition (2020)
17. Kingma, D.P., Ba, J.: Adam: A Method for Stochastic Optimization. In: International Conference on Learning Representations (2015)
18. Lewiner, T., Lopes, H., Vieira, A.W., Tavares, G.: Efficient Implementation of Marching Cubes’ Cases with Topological Guarantees. In: Journal of Graphics Tools (2003)
19. Li, T., Wen, X., Liu, Y.S., Su, H., Han, Z.: Learning Deep Implicit Functions for 3D Shapes with Dynamic Code Clouds. In: Conference on Computer Vision and Pattern Recognition (2022)
20. Lindell, D.B., Van Veen, D., Park, J.J., Wetzstein, G.: Bacon: Band-limited coordinate networks for multiscale scene representation. In: Conference on Computer Vision and Pattern Recognition (2022)
21. Liu, H.T.D., Williams, F., Jacobson, A., Fidler, S., Litany, O.: Learning smooth neural functions via lipschitz regularization. In: ACM SIGGRAPH (2022)
22. Mescheder, L., Oechsle, M., Niemeyer, M., Nowozin, S., Geiger, A.: Occupancy Networks: Learning 3D Reconstruction in Function Space. In: Conference on Computer Vision and Pattern Recognition. pp. 4460–4470 (2019)
23. Mezghanni, M., Bodrito, T., Boulkenafed, M., Ovsjanikov, M.: Physical simulation layer for accurate 3d modeling. In: Conference on Computer Vision and Pattern Recognition (2022)
24. Park, J.J., Florence, P., Straub, J., Newcombe, R., Lovegrove, S.: Deepsdf: Learning Continuous Signed Distance Functions for Shape Representation. In: Conference on Computer Vision and Pattern Recognition (2019)
25. Peng, S., Niemeyer, M., Mescheder, L., Pollefeys, M., Geiger, A.: Convolutional Occupancy Networks. In: European Conference on Computer Vision. pp. 523–540 (2020)
26. Ramasinghe, S., Lucey, S.: Beyond periodicity: towards a unifying framework for activations in coordinate-mlps. In: European Conference on Computer Vision (2022)
27. Ravi, N., Reizenstein, J., Novotny, D., Gordon, T., Lo, W.Y., Johnson, J., Gkioxari, G.: Accelerating 3d deep learning with pytorch3d. arXiv:2007.08501 (2020)
28. Remelli, E., Lukoianov, A., Richter, S., Guillard, B., Bagautdinov, T., Baque, P., Fua, P.: Meshsdf: Differentiable Iso-Surface Extraction. In: Advances in Neural Information Processing Systems (2020)
29. Saito, S., Huang, Z., Natsume, R., Morishima, S., Kanazawa, A., Li, H.: PIFu: Pixel-Aligned Implicit Function for High-Resolution Clothed Human Digitization. In: International Conference on Computer Vision (2019)
30. Saito, S., Simon, T., Saragih, J., Joo, H.: Pifuhd: Multi-Level Pixel-Aligned Implicit Function for High-Resolution 3D Human Digitization. In: Conference on Computer Vision and Pattern Recognition. pp. 84–93 (2020)
31. Shekarforoush, S., Lindell, D., Fleet, D.J., Brubaker, M.A.: Residual multiplicative filter networks for multiscale reconstruction. Advances in Neural Information Processing Systems (2022)
32. Sitzmann, V., Martel, J., Bergman, A., Lindell, D., Wetzstein, G.: Implicit Neural Representations with Periodic Activation Functions. In: Advances in Neural Information Processing Systems (2020)

33. Takikawa, T., Evans, A., Tremblay, J., Müller, T., McGuire, M., Jacobson, A., Fidler, S.: Variable bitrate neural fields. In: ACM SIGGRAPH (2022)
34. Takikawa, T., Litalien, J., Yin, K., Kreis, K., Loop, C., Nowrouzezahrai, D., Jacobson, A., McGuire, M., Fidler, S.: Neural geometric level of detail: Real-time rendering with implicit 3d shapes. In: Conference on Computer Vision and Pattern Recognition (2021)
35. Tancik, M., Srinivasan, P., Mildenhall, B., Fridovich-Keil, S., Raghavan, N., Singhal, U., Ramamoorthi, R., Barron, J., Ng, R.: Fourier features let networks learn high frequency functions in low dimensional domains. In: Advances in Neural Information Processing Systems (2020)
36. Venkatesh, R., Karmali, T., Sharma, S., Ghosh, A., Babu, R.V., Jeni, L.A., Singh, M.: Deep Implicit Surface Point Prediction Networks. In: International Conference on Computer Vision (2021)
37. Wang, P.S., Fu, X.M., Liu, Y., Tong, X., Liu, S.L., Guo, B.: Rolling guidance normal filter for geometric processing (2015)
38. Xu, Q., Wang, W., Ceylan, D., Mech, R., Neumann, U.: DISN: Deep Implicit Surface Network for High-Quality Single-View 3D Reconstruction. In: Advances in Neural Information Processing Systems (2019)
39. Yang, G., Benaim, S., Jampani, V., Genova, K., Barron, J., Funkhouser, T., Hariharan, B., Belongie, S.: Polynomial Neural Fields for Subband Decomposition and Manipulation. In: Advances in Neural Information Processing Systems (2022)
40. Yatagawa, T.: mcubes_pytorch: PyTorch Implementation for Marching Cubes (2020), https://github.com/tatsy/mcubes_pytorch/
41. Yifan, W., Rahmann, L., Sorkine-hornung, O.: Geometry-consistent neural shape representation with implicit displacement fields. In: International Conference on Learning Representations (2022)
42. Zhang, B., Nießner, M., Wonka, P.: 3dirl: Irregular latent grids for 3d generative modeling. In: Advances in Neural Information Processing Systems (2022)
43. Zhang, J., Deng, B., Hong, Y., Peng, Y., Qin, W., Liu, L.: Static/dynamic filtering for mesh geometry (2018)
44. Zhao, F., Wang, W., Liao, S., Shao, L.: Learning Anchored Unsigned Distance Functions with Gradient Direction Alignment for Single-View Garment Reconstruction. In: International Conference on Computer Vision (2021)

6 Proof of the band-limits of our network

Our network with N layers maps a latent code $\mathbf{l} \in \mathbb{R}^{d_l}$ and an input coordinate $\mathbf{x} \in \mathbb{R}^3$ to $N-1$ estimates of the SDF at this position, $f_\Omega(\mathbf{x}, \mathbf{l}, i)$ with $1 \leq i < N$. The input coordinate $\mathbf{x} \in \mathbb{R}^3$ is first encoded using sine layers

$$\mathbf{g}_i(\mathbf{x}) = \sin(\boldsymbol{\omega}_i \mathbf{x} + \boldsymbol{\phi}_i) \in \mathbb{R}^{d_h} \quad (7)$$

for $i = 0, \dots, N-1$, with $\boldsymbol{\omega}_i \in \mathbb{R}^{d_h \times 3}$, $\boldsymbol{\phi}_i \in \mathbb{R}^{d_h}$, and d_h the hidden dimension. Intermediate activations $\mathbf{z}_i \in \mathbb{R}^{d_h+d_l}$ and SDF outputs $f_\Omega(\mathbf{x}, \mathbf{l}, i) \in \mathbb{R}$ are defined as

$$\begin{aligned} \mathbf{z}_0 &= [\mathbf{g}_0(\mathbf{x}) \mid \mathbf{l}] \\ \mathbf{z}_i &= [\mathbf{g}_i(\mathbf{x}) \mid \mathbf{l}] \circ (\mathbf{W}_i \mathbf{z}_{i-1} + \mathbf{b}_i) \\ f_\Omega(\mathbf{x}, \mathbf{l}, i) &= \mathbf{W}_i^{out} \mathbf{z}_i + \mathbf{b}_i^{out}, \quad 1 \leq i < N. \end{aligned} \quad (8)$$

where \circ is the Hadamard product, $(\mathbf{W}_i, \mathbf{b}_i) \in \mathbb{R}^{(d_h+d_l) \times (d_h+d_l)} \times \mathbb{R}^{d_h+d_l}$ are the *linear layers* and $(\mathbf{W}_i^{out}, \mathbf{b}_i^{out}) \in \mathbb{R}^{1 \times (d_h+d_l)} \times \mathbb{R}$ are the *output layers*.

We here show that for a fixed latent code $\mathbf{l} \in \mathbb{R}^{d_l}$, the above formulation can be rewritten into a standard BACON network [20], and thus enjoys the same band-limits. The main intuition is to hardcode \mathbf{l} as a fixed component within the coordinate embeddings.

Let us first define $\alpha = \max(|\mathbf{l}|)$ the largest coefficient of \mathbf{l} in absolute scale, thus allowing us to write

$$\mathbf{l} = \alpha \sin(\bar{\mathbf{l}})$$

for some $\bar{\mathbf{l}} \in \mathbb{R}^{d_l}$. Using this expression of \mathbf{l} we define $\mathbf{g}'_i(\cdot)$ as

$$\mathbf{g}'_i(\mathbf{x}) = \sin([\boldsymbol{\omega}_i \mid 0] \mathbf{x} + [\boldsymbol{\phi}_i \mid \bar{\mathbf{l}}])$$

where $[\boldsymbol{\omega}_i \mid 0] \in \mathbb{R}^{(d_h+d_l) \times 3}$ means the concatenation of $\boldsymbol{\omega}_i$ with d_l zeros vectors $(0, 0, 0)$ along the row axis. By denoting $[1 \mid \alpha] \in \mathbb{R}^{d_h+d_l}$ the concatenation of d_h coefficients 1 followed by d_l coefficients α , we get

$$[\mathbf{g}_i(\mathbf{x}) \mid \mathbf{l}] = [1 \mid \alpha] \circ \mathbf{g}'_i(\mathbf{x}) \quad .$$

The multiplication by $[1 \mid \alpha]$ can be absorbed in the matrix multiplications. We define \mathbf{W}'_i and $\mathbf{W}_i'^{out}$ by scaling the last d_l columns of \mathbf{W}_i and \mathbf{W}_i^{out} by α :

$$\mathbf{W}'_i = \mathbf{W}_i \circ \begin{pmatrix} [1 \mid \alpha] \\ \dots \\ [1 \mid \alpha] \end{pmatrix} \quad (9)$$

$$\mathbf{W}_i'^{out} = \mathbf{W}_i^{out} \circ \begin{pmatrix} [1 \mid \alpha] \\ \dots \\ [1 \mid \alpha] \end{pmatrix} \quad (10)$$

As a result, by fixing \mathbf{l} , Equation (8) can be rewritten as a standard BACON network [20] with hidden dimension $d_h + d_l$ and parameters

$$\boldsymbol{\omega}'_i = [\boldsymbol{\omega}_i \mid 0] , \quad (11)$$

$$\boldsymbol{\phi}'_i = [\boldsymbol{\phi}_i \mid \bar{\mathbf{l}}] , \quad (12)$$

$$\mathbf{W}'_i = \mathbf{W}_i \circ \begin{pmatrix} [1 \mid \alpha] \\ \dots \\ [1 \mid \alpha] \end{pmatrix} , \quad (13)$$

$$\mathbf{b}'_i = \mathbf{b}_i , \quad (14)$$

$$\mathbf{W}_i'^{out} = \mathbf{W}_i^{out} \circ \begin{pmatrix} [1 \mid \alpha] \\ \dots \\ [1 \mid \alpha] \end{pmatrix} , \quad (15)$$

$$\mathbf{b}_i'^{out} = \mathbf{b}_i^{out} . \quad (16)$$

7 Hyperparameters

We set the maximum spatial frequency to $B = \sum_i B_i = 256$ and distribute the bandwidth as

- $B_0 = B/48$;
- $B_1 = B_2 = B_3 = B_4 = B/24$;
- $B_5 = B_6 = B_7 = B/16$;
- $B_8 = B_9 = B_{10} = B_{11} = B_{12} = B/8$.

Latent codes are of size $d_l = 256$ and coordinate embeddings of size $d_h = 256$, for a total layer width of 512. Our networks are trained for 10^6 steps with the Adam optimizer [17], and with a learning rate decreasing logarithmically from 10^{-2} to 10^{-4} . We use mini-batches of 4 shapes, each of them represented as 10k SDF samples at each iteration. We set the coarse sample weights to $\lambda_c = 10^{-2}$ in, and the regularizer weight to $\lambda_{reg} = 10^{-4}$.

We follow the SDF sampling strategy of [24] for querying ground truth samples. The fine samples used in \mathcal{L}_{sdf} are the top 5% that are the closest to the surface, remaining ones are the coarse ones.

The renderings of Fig. 8 were done using the mesh rasterization modules of PyTorch3D [27], with disabled backpropagation and at a resolution of 512*512 pixels.

8 Adding Eikonal regularization to *ReLU-net*

We added an Eikonal regularization [1] to a shallow *ReLU-net* network to test its effect on surface regularity. It consists in (softly) constraining the spatial gradient norms to be equal to 1 — as for a true SDF field. As shown in Figure 10, this does not fix surface artefacts. In addition, it is significantly slower to train because it requires the computation of second order gradients.

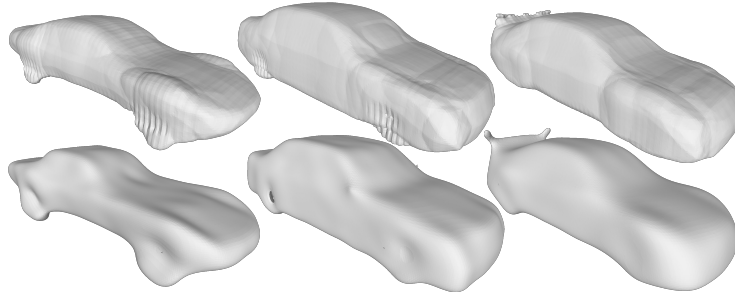


Fig. 10: **Eikonal regularization** on a 1-layer *ReLU-net* (**top**) still yields rough surfaces with many artefacts compared to our network at level $i = 1$ (**bottom**).

9 Setting the maximum bandwidth B

Layer #:	2			4			8			12		
Metric	CD	ED	SR	CD	ED	SR	CD	ED	SR	CD	ED	SR
Ours with Chairs												
$B = 64$	30.8	8.0	5.6	22.3	6.7	4.9	11.3	4.1	7.5	11.3	4.0	7.9
$B = 256$	14.3	5.4	7.8	10.1	4.0	7.8	8.3	3.4	8.3	8.3	3.4	8.4
$B = 1024$	14.9	5.2	12.6	8.7	3.6	11.7	8.2	3.4	15.9	8.2	3.4	17.9

Table 2: **Unseen test chairs:** Chamfer Distances (CD), Earth mover’s Distances (ED) and Surface Roughness (SR) for varying maximum bandwidth values B (by default $B = 256$ in our paper). With $B = 64$ surfaces are smoother (lower SR) but less precise (higher CD and ED). With $B = 1024$, they fit more closely the ground truth (lower CD and ED) but show many local artefacts (higher SR), as shown on Figure 11.

In Figure 11 and Tab. 2 we train variants our network on chairs with a maximum bandwidth $B = 64$, $B = 1024$, and compare to our default value of $B = 256$ on the test set. With a lower bandwidth, the level of detail increases more gradually, but reconstruction accuracy is decreased. A higher bandwidth leads to metrics saturating quicker, and thus a less progressive increase in details, as well as high frequency artefacts on the reconstructed surfaces.

In Figure 12 we show an example of increasing the level of detail with our network when $B = 256$, with $B_0 = B/48$; $B_1 = B_2 = B_3 = B_4 = B/24$; $B_5 = B_6 = B_7 = B/16$ and $B_8 = B_9 = B_{10} = B_{11} = B_{12} = B/8$.

10 Multi-scale *ReLU-net*

We extended *ReLU-net* into a multi-scale version. In the spirit of our own architecture, we add one output layer per hidden layer. The resulting network

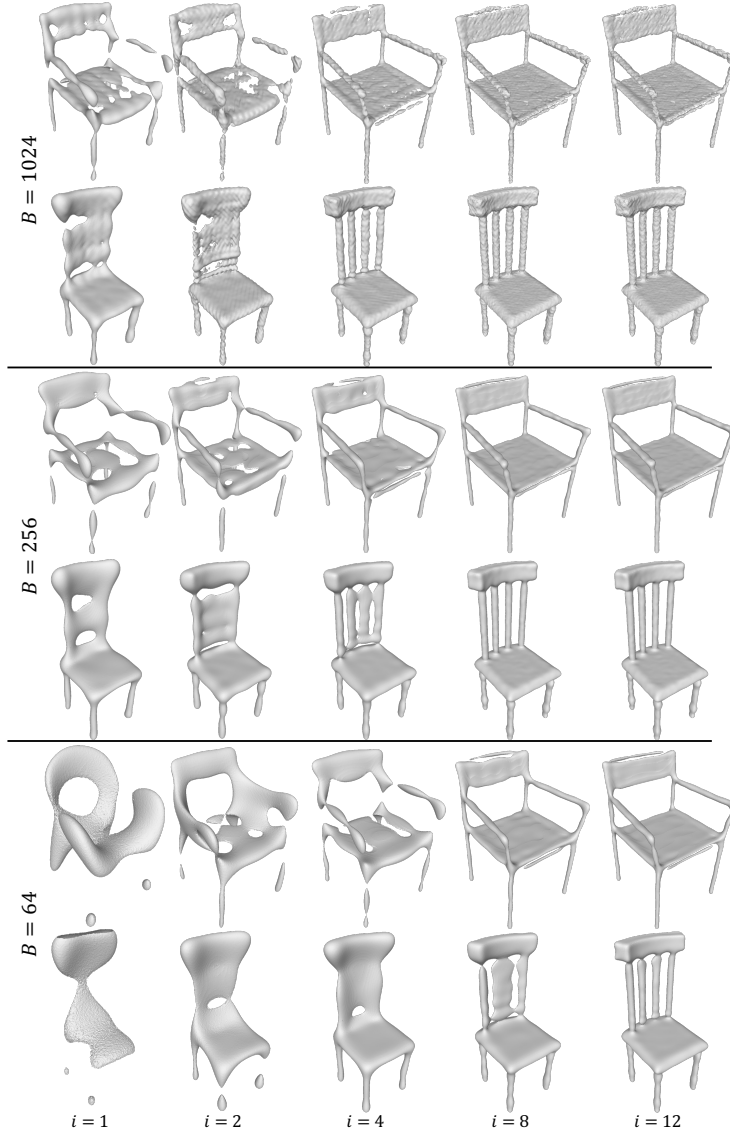
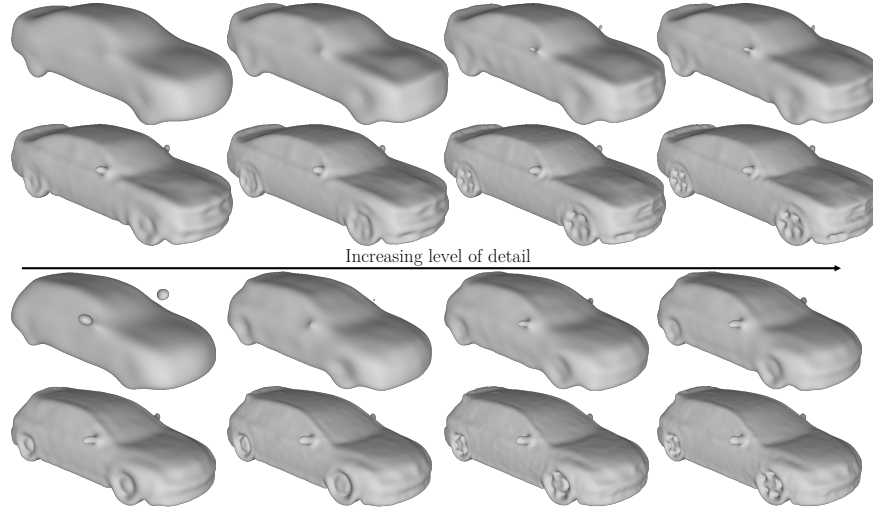


Fig. 11: **Setting the maximum bandwidth B :** we compare reconstructed chairs with a high maximum frequency ($B = 1024$, **top**), our default value ($B = 256$, **middle**), and a low maximum frequency ($B = 64$, **bottom**), at different levels of detail i . With $B = 1024$, surfaces are not smooth and show high frequency artefacts. With $B = 64$, the details increase more gradually, but the highest level of detail still shows over-smoothed shapes.

Fig. 12: **Increasing level of detail** with our model on cars, from $i = 1$ to $i = 8$.

Layer #:	2			4			8			12		
Metric	CD	ED	SR	CD	ED	SR	CD	ED	SR	CD	ED	SR
	Chairs											
<i>MS-ReLU</i> (single net.)	17.4	5.5	10.1	8.7	3.6	10.2	8.6	3.4	10.3	8.5	3.4	11.4
<i>ReLU-net</i> (1 / column)	10.0	3.9	13.0	9.1	3.7	12.4	8.8	3.6	12.5	9.3	3.6	13.2
Ours (single net.)	14.3	5.4	7.8	10.1	4.0	7.8	8.3	3.4	8.3	8.3	3.4	8.4

Table 3: **Unseen test chairs:** Chamfer Distances (CD), Earth mover’s Distances (ED) and Surface Roughness (SR). Lower values indicate better results for all metrics. *MS-ReLU*, which is a multiscale version of *ReLU-net*, performs slightly better than the latter. Our network is however consistently smoother (SR) while achieving comparable accuracy (CD, ED).

thus provides multiple SDFs outputs from a single network and latent code, each corresponding to a depth level. We refer to this method as *MS-ReLU*. It solves one issue of *ReLU-net* and *Sin-net*, by mapping a single latent code to multiple surface estimates, without requiring to put different latent spaces in correspondence.

However, it still suffers from the same artefacts as *ReLU-net* with rougher surfaces, as reported in Table 3 on test chairs. Moreover, it provides no explicit control of the bandwidth, and the coarse to fine hierarchy is only tied to the increasing network capacity.

11 Decreasing Marching Cubes Resolution

Decreasing marching cubes resolution is a trivial baseline for reducing the level of detail and computation time. However, as shown in Table 4, this solution negatively impacts the reconstruction accuracy. A grid coarse grid resolution yields very inaccurate shapes. By comparison, our method provides better shape approximations.

	MC=64 ³	MC=256 ³
Layer # : 1	2.94	2.89
2	1.54	1.26
3	1.46	1.02
4	1.47	0.90
5	1.46	0.84
6	1.68	0.79
7	1.78	0.77
8	1.89	0.75
9	1.93	0.74
10	1.90	0.72
11	1.91	0.72
12	1.94	0.72

Table 4: **Chamfer Distance (CD) with marching cubes resolutions (MC) of 64 and 256**, on the chairs dataset. A low marching cubes resolution always yield more inaccurate reconstructions.

12 Additional Qualitative Results

In Figure 13 we show qualitative results when training our network on a dataset of human body meshes. Figure 14 displays additional results on the chairs, cars and airplanes categories. In both cases, our pipeline accurately captures details at high resolution, while also yielding smooth surfaces at low resolutions.

13 Additional Comparisons with the Baselines

In Tables 5 and 6 we report metrics at all depths levels for our method and the two baselines *ReLU-net* and *Sin-net* on both unseen test shapes and training ones. Their interpretation is consistent with the ones reported in the main text: our pipeline achieves comparable accuracy levels, while being consistently smoother.

In Figures 15 and 16 we show unseen cars and chairs reconstructed by *Sin-net*, *ReLU-net* and our network.

Metric: Chamfer Distance (CD, ↓)

Layer # :	1	2	3	4	5	6	7	8	9	10	11	12
	Cars											
<i>Sin-net</i> (1 / column)	8.0	7.9	7.1	6.8	6.4	6.5	10.3	10.5	10.8	6.6	8.8	10.8
<i>ReLU-net</i> (1 / column)	7.6	7.7	6.3	6.0	8.6	6.0	6.3	6.3	6.0	6.0	6.1	6.1
Ours (single net.)	11.0	8.1	7.4	7.0	6.7	6.6	6.3	6.3	6.3	6.3	6.3	6.3
	Chairs											
<i>Sin-net</i> (1 / column)	14.9	14.9	13.9	13.4	13.2	12.9	16.8	10.7	11.9	10.5	12.4	12.7
<i>ReLU-net</i> (1 / column)	13.1	10.0	9.4	9.1	10.5	9.9	8.5	8.8	8.5	9.5	8.8	9.3
Ours (single net.)	25.3	14.3	11.3	10.1	9.2	8.6	8.5	8.3	8.3	8.3	8.3	8.3
	Airplanes											
<i>Sin-net</i> (1 / column)	5.4	4.5	3.9	3.6	3.1	4.3	3.3	2.9	3.2	3.0	4.5	5.2
<i>ReLU-net</i> (1 / column)	30.5	3.0	3.0	2.7	2.7	2.8	2.7	2.6	3.1	2.5	2.5	2.4
Ours (single net.)	12.2	5.8	4.4	3.8	3.2	2.9	2.8	2.7	2.7	2.7	2.7	2.7

Metric: Earth mover's Distance (ED, ↓)

Layer # :	1	2	3	4	5	6	7	8	9	10	11	12
	Cars											
<i>Sin-net</i> (1 / column)	4.0	3.9	3.6	3.5	3.4	3.3	3.5	3.5	3.5	3.3	3.5	3.5
<i>ReLU-net</i> (1 / column)	3.2	2.9	2.8	2.8	2.8	2.7	2.7	2.7	2.7	2.7	2.7	2.7
Ours (single net.)	3.8	3.2	3.0	2.9	2.8	2.8	2.8	2.8	2.8	2.8	2.8	2.8
	Chairs											
<i>Sin-net</i> (1 / column)	4.8	5.0	4.8	4.6	4.6	4.3	4.8	4.9	4.7	4.8	5.7	6.4
<i>ReLU-net</i> (1 / column)	4.5	3.9	3.8	3.7	3.8	3.8	3.5	3.6	3.4	3.7	3.5	3.6
Ours (single net.)	7.0	5.4	4.4	4.0	3.7	3.5	3.4	3.4	3.4	3.4	3.4	3.4
	Airplanes											
<i>Sin-net</i> (1 / column)	3.3	3.3	2.7	2.5	2.1	2.2	2.3	2.1	2.1	1.8	15.7	16.1
<i>ReLU-net</i> (1 / column)	3.3	2.0	1.9	2.0	1.6	1.8	1.6	1.8	1.9	1.6	1.6	1.6
Ours (single net.)	4.3	3.0	2.7	2.3	1.9	1.7	1.6	1.5	1.5	1.6	1.5	1.5

Metric: Surface Regularity (SR, ↓)

Layer # :	1	2	3	4	5	6	7	8	9	10	11	12
	Cars											
<i>Sin-net</i> (1 / column)	9.5	9.5	9.8	9.9	9.8	9.5	9.7	9.7	9.6	10.4	10.1	9.6
<i>ReLU-net</i> (1 / column)	11.7	11.2	11.1	10.9	10.8	11.1	10.7	10.9	11.0	11.0	11.1	11.4
Ours (single net.)	4.9	5.5	5.9	6.1	6.4	6.6	6.9	7.1	7.2	7.3	7.3	7.3
	Chairs											
<i>Sin-net</i> (1 / column)	13.2	13.0	12.2	12.0	12.6	13.2	14.2	16.0	14.4	13.9	18.8	19.0
<i>ReLU-net</i> (1 / column)	14.7	13.0	12.6	12.4	12.6	12.3	12.5	12.5	12.8	13.1	13.1	13.2
Ours (single net.)	6.8	7.8	7.7	7.8	7.9	8.1	8.2	8.3	8.4	8.4	8.4	8.4
	Airplanes											
<i>Sin-net</i> (1 / column)	15.9	14.0	12.9	13.7	13.6	13.7	13.6	14.7	14.1	14.8	15.2	16.1
<i>ReLU-net</i> (1 / column)	15.3	15.0	14.6	14.5	15.2	14.6	14.9	15.5	14.4	16.2	16.5	14.8
Ours (single net.)	9.6	12.2	12.8	13.0	13.4	13.7	13.8	14.1	14.4	14.4	14.5	14.5

Table 5: **Unseen test shapes:** Chamfer Distances (CD), Earth mover's Distances (ED) and Surface Regularity (SR), for all depths. Lower values indicate better results for all metrics. We achieve comparable best accuracy (CD, ED) while being consistently smoother (SR) than the best baseline (*ReLU-net*).

Metric: Chamfer Distance (CD, ↓)

Layer # :	1	2	3	4	5	6	7	8	9	10	11	12
	Cars											
<i>Sin-net</i> (1 / column)	10.7	10.7	9.8	9.3	8.2	7.9	7.6	7.5	7.3	8.4	10.6	10.7
<i>ReLU-net</i> (1 / column)	7.8	6.1	5.8	5.7	5.7	5.6	5.7	5.7	5.7	5.7	5.7	5.7
Ours (single net.)	10.4	7.5	6.7	6.4	6.0	5.9	5.7	5.7	5.6	5.6	5.6	5.6
	Chairs											
<i>Sin-net</i> (1 / column)	29.0	27.5	13.1	12.2	9.1	7.9	7.1	6.2	6.6	6.0	11.9	14.9
<i>ReLU-net</i> (1 / column)	11.1	7.9	6.8	6.4	6.2	6.0	5.9	6.0	5.8	5.8	5.9	6.1
Ours (single net.)	17.8	9.1	7.8	7.0	6.4	6.0	5.8	5.7	5.6	5.6	5.6	5.6
	Airplanes											
<i>Sin-net</i> (1 / column)	21.3	21.5	7.5	6.1	6.2	5.8	6.2	6.0	6.0	5.4	7.6	9.1
<i>ReLU-net</i> (1 / column)	7.7	2.7	2.3	2.3	2.2	2.4	2.3	2.3	2.2	2.2	2.4	2.1
Ours (single net.)	15.0	4.0	3.0	2.5	2.2	2.1	2.0	1.9	1.8	1.8	1.8	1.8

Metric: Earth mover's Distance (ED, ↓)

Layer # :	1	2	3	4	5	6	7	8	9	10	11	12
	Cars											
<i>Sin-net</i> (1 / column)	4.2	4.2	3.9	3.8	3.6	3.5	3.4	3.4	3.4	3.6	4.0	3.6
<i>ReLU-net</i> (1 / column)	3.1	2.7	2.7	2.6	2.6	2.6	2.6	2.6	2.6	2.6	2.6	2.6
Ours (single net.)	3.6	3.0	2.9	2.8	2.7	2.6	2.6	2.6	2.6	2.6	2.6	2.6
	Chairs											
<i>Sin-net</i> (1 / column)	14.7	14.0	7.5	6.5	5.1	4.4	4.1	3.6	3.3	3.0	6.9	8.0
<i>ReLU-net</i> (1 / column)	4.2	3.5	3.1	2.9	2.9	2.8	2.7	2.8	2.7	2.7	2.7	2.8
Ours (single net.)	5.6	3.7	3.3	3.1	3.0	2.8	2.8	2.7	2.7	2.7	2.7	2.7
	Airplanes											
<i>Sin-net</i> (1 / column)	4.2	4.3	2.1	1.7	1.6	1.5	1.5	1.5	1.5	1.4	2.2	2.4
<i>ReLU-net</i> (1 / column)	2.2	1.5	1.4	1.4	1.3	1.3	1.3	1.3	1.3	1.3	1.3	1.3
Ours (single net.)	4.4	2.1	1.7	1.5	1.3	1.2	1.1	1.0	1.0	1.0	1.0	1.0

Metric: Surface Regularity (SR, ↓)

Layer # :	1	2	3	4	5	6	7	8	9	10	11	12
	Cars											
<i>Sin-net</i> (1 / column)	6.8	6.8	7.4	7.7	8.1	8.5	8.8	8.8	9.0	8.4	13.8	14.8
<i>ReLU-net</i> (1 / column)	9.7	9.3	9.3	9.2	9.5	9.5	9.6	9.2	9.5	9.6	9.6	9.5
Ours (single net.)	4.9	5.6	6.0	6.3	6.7	7.0	7.3	7.6	7.7	7.7	7.8	7.8
	Chairs											
<i>Sin-net</i> (1 / column)	9.6	9.5	9.0	9.0	9.4	9.8	10.3	11.3	10.8	10.9	15.7	15.9
<i>ReLU-net</i> (1 / column)	12.6	10.9	10.5	10.4	10.6	10.4	10.6	10.5	10.8	11.0	11.1	10.9
Ours (single net.)	6.8	7.6	7.7	7.9	8.1	8.3	8.4	8.6	8.7	8.8	8.8	8.8
	Airplanes											
<i>Sin-net</i> (1 / column)	13.8	13.8	14.1	14.4	14.7	14.9	15.2	15.4	15.6	15.8	17.8	19.3
<i>ReLU-net</i> (1 / column)	17.4	16.6	16.5	16.6	16.7	16.7	16.9	16.8	16.8	17.0	16.9	17.1
Ours (single net.)	9.7	12.2	12.8	13.0	13.3	13.6	13.8	14.2	14.5	14.6	14.6	14.6

Table 6: **Training shapes:** Chamfer Distances (CD), Earth mover's Distances (ED) and Surface Regularity (SR), for all depths. Lower values indicate better results for all metrics. We achieve comparable best accuracy (CD, ED) while being consistently smoother (SR) than the best baseline (*ReLU-net*).

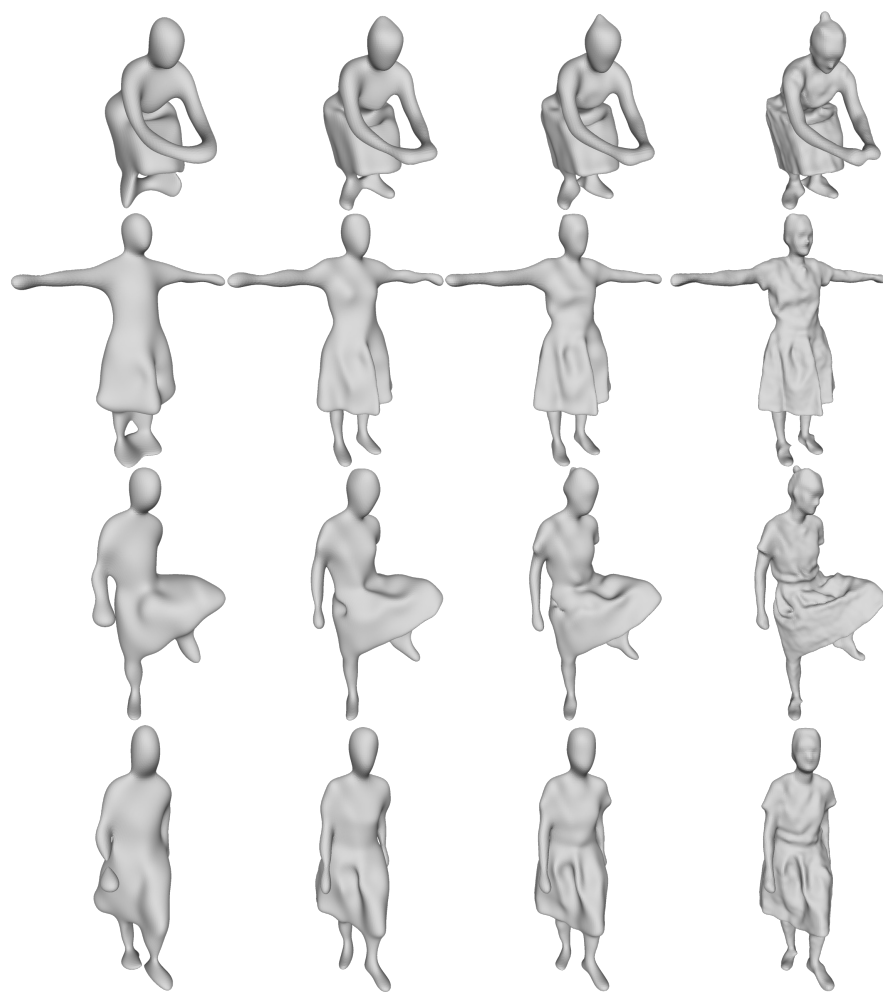


Fig. 13: **Human Body Reconstructions** with varying levels of detail, at resolutions $i = 1, 2, 4$ and 12 .

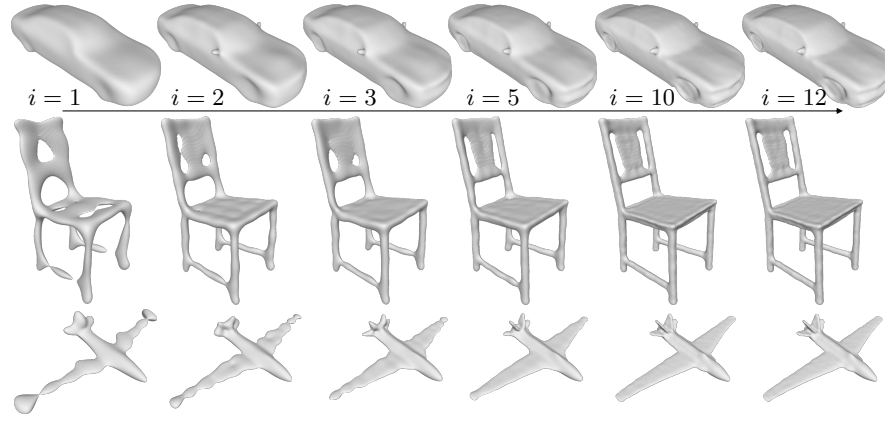


Fig. 14: **Test Shape Reconstructions** with varying levels of detail. The lowest possible level of detail ($i = 1$) is smooth and already captures a very coarse structure of the shape. As i increases, more details appear (up to a point of saturation).

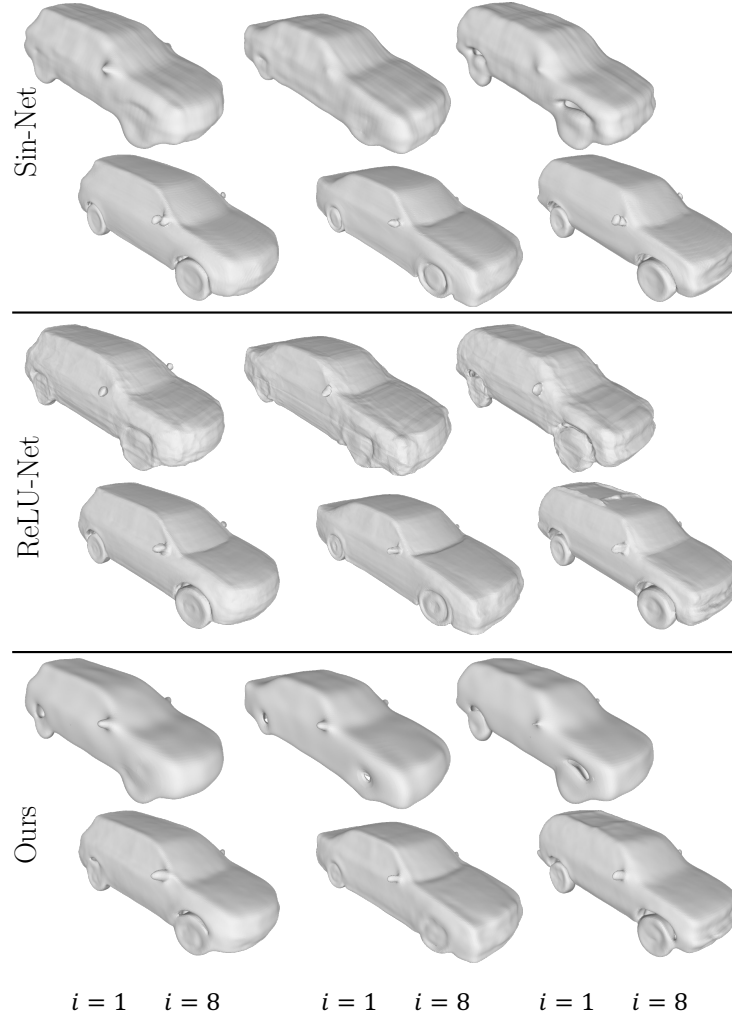


Fig. 15: **Unseen test cars** reconstructed by *Sin-net* (**top**), *ReLU-net* (**middle**) and our network (**bottom**), at levels of detail $i = 1$ and $i = 8$.

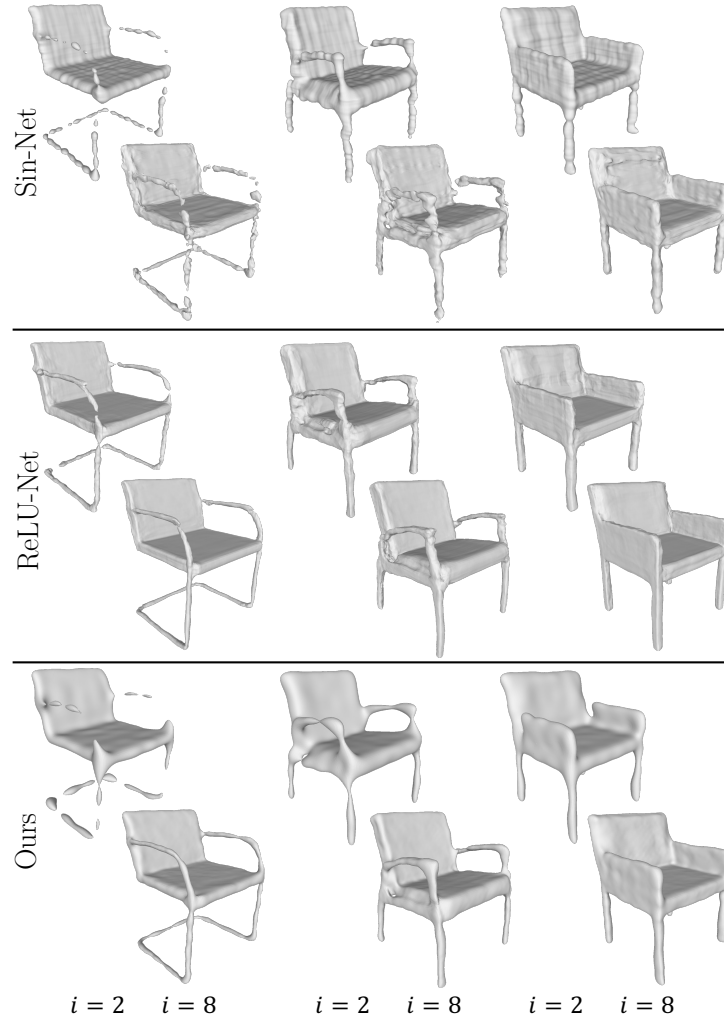


Fig. 16: **Unseen test chairs** reconstructed by *Sin-net* (**top**), *ReLU-net* (**middle**) and our network (**bottom**), at levels of detail $i = 2$ and $i = 8$.